A semiconductor laser device for the generation of surface-plasmons upon electrical injection

A. Bousseksou[1], **R. Colombelli**[1*], **A. Babuty**[2], **Y. De Wilde**[2*], **Y. Chassagneux**[1], **C. Sirtori**[3], **G. Patriarche**[4], **G. Beaudoin**[4], **I. Sagnes**[4]

[1] *Institut d'Electronique Fondamentale, Université Paris-Sud and CNRS, UMR8622, 91405 Orsay, France*

[2] *Institut Langevin, ESPCI ParisTech, CNRS UMR 7587, Laboratoire d'Optique Physique, 10 rue Vauquelin, 75231 Paris, France.*

[3] *Laboratoire MPQ, Université Paris Diderot and CNRS, UMR7612, 75013 Paris, France*

[4] *CNRS/LPN, Laboratoire de Photonique et de Nanostructures, Marcoussis, France*

Corresponding authors: raffaele.colombelli@u-psud.fr, dewilde@optique.espci.fr

Abstract: Surface plasmons are electromagnetic waves originating from electrons and light oscillations at metallic surfaces. Since freely propagating light cannot be coupled directly into surface-plasmon modes, a compact, semiconductor electrical device capable of generating SPs on the device top metallic surface would represent an advantage: not only SP manipulation would become easier, but Au-metalized surfaces can be easily functionalized for applications. Here, we report a demonstration of such a device. The direct proof of surface-plasmon generation is obtained with apertureless near-field scanning optical microscopy, which detects the presence of an intense, evanescent electric field above the device metallic surface upon electrical injection.

© 2009 Optical Society of America

References and links

1. T. W. Ebbesen, C. Genet, and S. I. Bozhevolnyi, "Surface plasmon circuitry," Phys. Today **61**, 44–50 (2008).
2. S. A. Maier, *Plasmonics: fundamentals and applications* (Springer, 2007).
3. W. L. Barnes, A. Dereux, and T. W. Ebbesen, "Surface plasmon subwavelength optics," Nature (London) **424**, 824–830 (2003).
4. F. Lopez-Tejeira, S. G. Rodrigo, L. Martn-Moreno, F. J. Garca-Vidal, E. Devaux, T. W. Ebbesen, J. R. Krenn, I. P. Radko, S. I. Bozhevolnyi, M. U. Gonzlez, J. C. Weeber, and A. Dereux, "Efficient unidirectional nanoslit couplers for surface-plasmons," Nat. Phys. **3**, 324–328 (2007).
5. T. Holmgaard, S. I. Bozhevolnyi, L. Markey, and A. Dereux, "Dielectric-loaded surface-plasmon polariton waveguides at telecommunication wavelengths: excitation and characterization," Appl. Phys. Lett. **92**, 011124 (2008).
6. F. Zenhausern, M. P. O'Boyle, and H. K. Wikramasynghe, "Apertureless near-field optical microscope," Appl. Phys. Lett. **65**, 1623–1625 (2004).
7. R. Bachelot, P. Gleyzes, and A. C. Boccara, "Near field optical microscopy by local perturbation of a diffraction spot," Microsc. Microanal. Microstruct. **5**, 389–397 (2004).
8. M. I. Stockman, "Nanofocusing of Optical Energy in Tapered Plasmonic Waveguides," Phys. Rev. Lett. **93**, 137404 (2004).
9. S. A. Maier, P. G. Kik, and H. A. Atwater, "Optical pulse propagation in metal nanoparticle chain waveguides," Phys. Rev. B **67**, 205402 (2003).
10. K. F. MacDonald, Z. L. Sámson, M. I. Stockman, and N. I. Zheludev, "Ultrafast plasmonics," Nat. Photon **3**, 53–58 (2009).

11. A. Degiron, P. Berini, and D. R. Smith, "Guiding light with long-range plasmons," Opt. Photon. News **19**, 28–34 (2008).

12. J. Y. Laluet, E. Devaux, C. Genet, T. W. Ebbesen, J. C. Weeber, and A. Dereux, "Optimization of surface plasmons launching from subwavelength hole arrays: modelling and experiments," Opt. Express **15**, 3488–3495 (2007).

13. D. J. Bergman and M. I. Stockman, "Surface Plasmon Amplification by Stimulated Emission of Radiation: Quantum Generation of Coherent Surface Plasmons in Nanosystems," Phys. Rev. Lett. **90**, 027402 (2003).

14. D. M. Koller, A. Hohenau, H. Ditlbacher, N. Galler, F. Reil, F. R. Aussenegg, A. Leitner, E. J. W. List, and J. R. Krenn, "Organic plasmon-emitting diode," Nat. Photon. **2**, 684–687 (2008).

15. M. Bahriz, V. Moreau, J. Palomo, R. Colombelli, D. Austin, J. Cockburn, L. Wilson, A. Krysa, and J. Roberts, "Room-temperature operation of $\lambda = 7.5$ μm surface-plasmon quantum cascade lasers," Appl. Phys. Lett. **88**, 181103 (2006).

16. C. Gmachl, F. Capasso, D. L. Sivco, and A. Y. Cho, "Recent progress in quantum cascade lasers and applications," Rep. Prog. Phys. **64**, 1533–1601 (2001).

17. J. M. Montgomery and S. K. Gray, "Enhancing surface plasmon polariton propagation lengths via coupling to asymmetric waveguide structures," Phys. Rev. B **77**, 125407 (2008).

18. A. Bousseksou, V. Moreau, R. Colombelli, C. Sirtori, G. Patriarche, O. Mauguin, L. Largeau, G. Beaudoin, and I. Sagnes, "Surface-plasmon distributed-feedback mid-infrared quantum cascade lasers based on hybrid plasmon/air-guided modes," IEEE Electron. Lett. **44**, 807–808 (2008).

19. The finite elements solver "Comsol Multiphysics" has been employed for the simulations. Bloch-periodic boundary conditions where implemented.

20. V. Moreau, M. Bahriz, R. Colombelli, R. Perahia, O. J. Painter, L. R. Wilson, and A. B. Krysa, "Demonstration of air-guided quantum cascade lasers without top claddings," Opt. Express **15**, 14861–14869 (2007).

21. S. Kumar, B. S. Williams, Q. Qin, A. W. M. Lee, and Q. Hu, "Surface-emitting distributed feedback terahertz quantum-cascade lasers in metal-metal waveguides," Opt. Express **15**, 113–128 (2007).

22. J. A. Fan, M. A. Belkin, F. Capasso, S. Khanna, M. Lachab, and A. G. D. E. H. Linfield, "Surface emitting terahertz quantum cascade laser with a double-metal waveguide," Opt. Express **14**, 11672–11680 (2007).

23. O. Demichel, L. Mahler, t. Losco, C. Mauro, R. Green, A. Tredicucci, J. Xu, F. Beltram, H. E. Beere, D. A. Ritchie, and V. Tamosinuas, "Surface plasmon photonic structures in terahertz quantum cascade lasers." Opt. Express **14**, 5335–5345 (2006).

24. H. Ditlbacher, N. Galler, D. M. Koller, A. Hohenau, A. Leitner, F. R. Aussenegg, and J. R. Krenn, "Coupling dielectric waveguide modes to surface-plasmon polaritons," Opt. Express **16**, 10455–10464 (2008).

25. Y. De Wilde, F. Formanek, R. Carminati, B. Gralak, P. A. Lemoine, K. Joulain, J. P. Mulet, Y. Chen, and J. J. Greffet, "Thermal radiation scanning tunnelling microscopy," Nature **444**, 740–743 (2006).

26. G. Wurtz, R. Bachelot, and P. Royer, "Imaging a GaAlAs laser diode in operation using apertureless scanning near-field optical microscopy," Eur. Phys. J.: Appl. Phys. **5**, 269–275 (1999).

27. N. Yu, L. Diehl, E. Cubukcu, C. Pflgl, D. Bour, S. Corzine, J. Zhu, G. Hofler, K. B. Crozier, and F. Capasso, "Near-field imaging of quantum cascade laser transverse modes," Opt. Express **15**, 13227–13235 (2007).

28. V. Moreau, M. Bahriz, R. Colombelli, P. A. Lemoine, Y. De Wilde, L. R. Wilson, and A. B. Krysa, "Direct imaging of a laser mode via midinfrared near-field microscopy," Appl. Phys. Lett. **90**, 201114 (2007).

29. J. B. Pendry, L. Martín-Moreno, and F. J. Garcia-Vidal, "Mimicking Surface Plasmons with Structured Surfaces," Science **305**, 847–848 (2004).

30. C. R. Williams, S. R. Andrews, S. A. Maier, A. I. F.-D. L. Martín-Moreno, and F. J. Garcia-Vidal, "Highly confined guiding of terahertz surface plasmon polaritons on structured metal surfaces," Nat. Photon. **2**, 175–179 (2008).

1. Introduction

Surface plasmons (SP) are electromagnetic modes localized at the interface between a metal and a dielectric. Recently this field of research has experienced intense activity [1, 2, 3] thanks to the development of sophisticated techniques for surface patterning [4, 5] and for probing the electromagnetic near-field of such surfaces [6, 7]. Besides applications to data storage [8], ultra-sensitive detection via field-enhancement, and micro/nano-optics for telecommunications [9, 10, 11], a great deal of activity is devoted to the development of active surface-plasmon components (couplers and modulators, for instance)[10, 12]. In particular, generating surface plasmons with a compact device is challenging [2]. SPs on unstructured surfaces cannot be optically excited unless the missing momentum between free photons and SPs of the same frequency is provided. A compact, semiconductor electrical device capable of generating SPs on the device top metallic surface would therefore represent an advantage.

A way forward to surface-plasmon (SP) generation consists in coupling the SP mode with

a material exhibiting optical emission or - even better - optical gain [13]. At visible wavelengths ($\approx$ 500 nm) organic light emitting diodes (OLED) support SP modes, as reported in Ref. [14]. However, the strong surface-plasmon attenuation along the propagation direction at short wavelengths makes the use of SPs for optical confinement disadvantageous in active devices at $\lambda \approx 1\ \mu$m. The use of SPs for semiconductor lasers becomes however possible in the mid-infrared [8 μm $< \lambda <$ 24 μm] [15]. Quantum cascade (QC) lasers are semiconductor lasers operating in this wavelength range [16]. In these devices the optical gain develops between quantized conduction band states and therefore it exists only when the electric-field is perpendicular to the plane of the layers (TM polarization). As a consequence, surface-plasmons can be exploited for waveguiding [15]. However, while it is generally assumed that SPs are electrically generated in the aforementioned systems, unfortunately they are not accessible from the air-side. This has prevented to date their direct observation via near-field microscopy, and their manipulation is especially complex.

We demonstrate a novel route towards SP guiding and generation in semiconductor laser systems operating under electrical injection. We give an experimental proof at $\lambda \approx 7.5\ \mu$m, but our strategy is general and a similar approach should be applicable in the near-IR and in the visible. We have in fact identified a configuration of the top metal that sustains new modes with extremely low propagation losses with respect to standard SPs. The waveguide is asymmetric as the active core is cladded between a top metal and a substrate with a lower index of refraction [17]. Periodically patterning the top metallic contact of the device substantiates the existence of these low loss surface-plasmon modes. The application of this concept to mid-IR QC lasers allows us to add useful functionalities to the devices (single mode emission). But most importantly, we prove that these SP modes can "tunnel" through the thicker-than-skin-depth metal layer and they can be detected on the device surface. The SP at the top air-metal interface profits now from the optical gain experienced by the SP on the other semiconductor side, as unambiguously confirmed by near-field characterizations of the devices during operation.

2. Optical stop-band, losses and field plots

Our model system is schematized in Fig.1(a), showing a longitudinal cross-section of an asymmetric semiconductor waveguide with a metallic top grating. The system is considered infinite in the y-direction. The layer thicknesses, indexes and the grating period (Λ), depend on the device emission wavelength (λ). In the rest of this work λ will be set at 7.5 μm, the wavelength of the laser studied [18]. The grating duty-cycle (DC) is defined as 0% for no metallization, and 100% for full metallization. Furthermore, in the rest of this paper we will employ reduced units for frequency (λ/Λ) and wavevector ($k/(2\pi/\Lambda)$). This is correct when operating well below the plasma frequency (infrared region), where the surface-plasmon dispersion is close to the light line, and the effect of the dispersion on the effective index of the waveguided modes can be neglected. When operating at shorter wavelengths (near-infrared and visible), this effect cannot be neglected anymore. However, this regime is beyond the scope of this paper and for this reason we opted for this simplification.

The photonic band structure of the infinite system is obtained by solving the 2D Helmoltz equation in a single unit cell (one period of the grating), with Bloch periodic boundary conditions [19]. The band-structure in reduced frequency and wavevector units for a 50% DC grating (not shown) shows that the metal periodic patterning provides enough feedback to introduce a stop-band at the band-edge, around the 1st order Bragg condition. For $\lambda = 7.5\ \mu$m, the wavelength separation between the two modes (labeled #1 and #2 in the rest of the paper) for a 50% DC grating is reasonably large, $\approx$ 40 nm.

The behavior of the system as a function of the grating DC is shown in Figs.1(b) and 1(c), which report the wavelength of modes #1 and #2, and the corresponding losses, from DC=0%
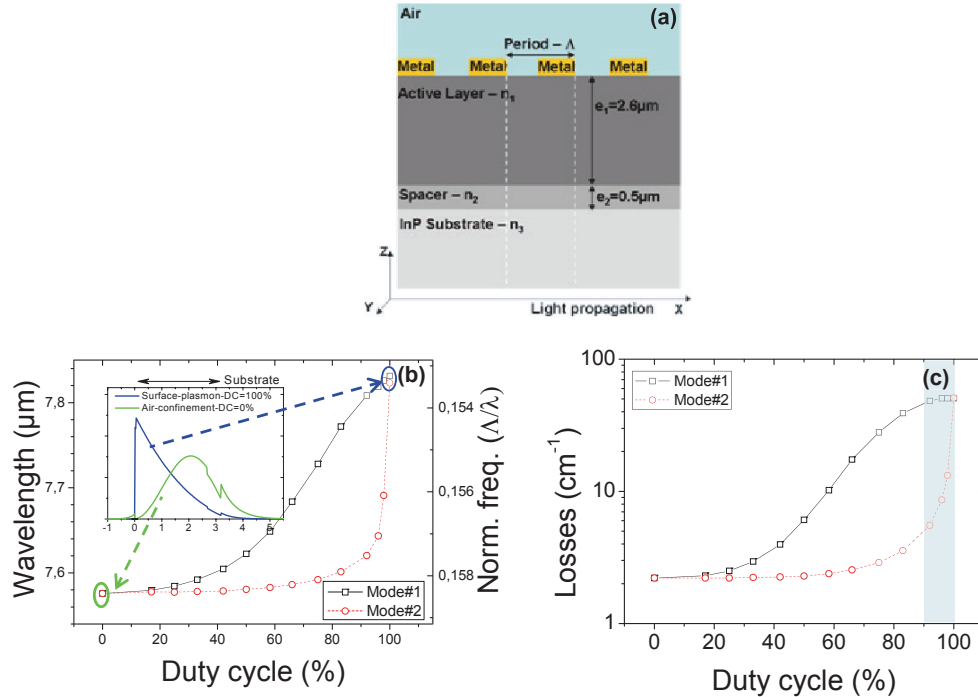
Fig. 1. Device scheme and modeling of the losses and emission wavelength. (a) Schematic cross section of the investigated waveguide system, which is considered infinite in the y-direction. The thicknesses are given for the case of a $\lambda = 7.5$ μm QC laser in the In-GaAs/AlInAs system. (b) Calculated wavelength of modes #1 and #2 as a function of the grating DC for a grating period $\Lambda = 1.2$ μm. DC=0% corresponds to no metallization on the device top surface. DC=100% corresponds to full, unpatterned metallization. Inset: calculated 1D waveguide modes for the two extreme cases of DC=0% and DC=100%. (c) Calculated losses per unit of length for modes #1 and #2 as a function of the grating duty cycle (DC). The losses of mode #2 are stable for almost all DC values. The refractive indexes of the layers composing the QC laser and used for the calculation are: $n_{active-region} = 3.269 + i*6.72x10^{-5}$, $n_{InP-substrate} = 3.055 + i*2.738x10^{-4}$, $n_{InGaAs-cladding} = 3.345 + i*2.342x10^{-4}$, and $n_{gold} = 7.8 + i*54.6$

(air-guided devices) to DC=100% (full top metallization, standard surface-plasmon guiding). When the frequency degeneracy is lifted by the metal patterning (Fig.1(b)), the maximum mode splitting is obtained at DC 90%. Note: while the wavelength of mode #1 smoothly increases from DC=0 to DC=100%, the wavelength of mode #2 is very stable up to DC 80%.

Figure 1(c) shows the propagation losses for modes #1 and #2 as a function of the grating DC. For DC=0%, the modes are degenerate, and bound by the air and substrate dielectric. The losses originate from free-carrier absorption in the semiconductor layers [20]. For DC=100% the modes are degenerate too, and they are standard surface-plasmons. Their losses are high ($\alpha \approx 50$ cm^{-1}). The presence of the grating breaks the degeneracy and introduces mode mixing: hybrid SP-air guided modes now appear. Mode #1 exhibits monotonically increasing losses. Mode #2 instead shows stable low losses up to extremely large DC values. At DC 80% the calculated loss difference ($\delta\alpha$) between the two modes is $\delta\alpha = 35$ cm^{-1}, thus suggesting that stable single-mode operation should be easily obtained for a surface-plasmon distributed-feedback (DFB) laser relying on this principle. This is a very important difference
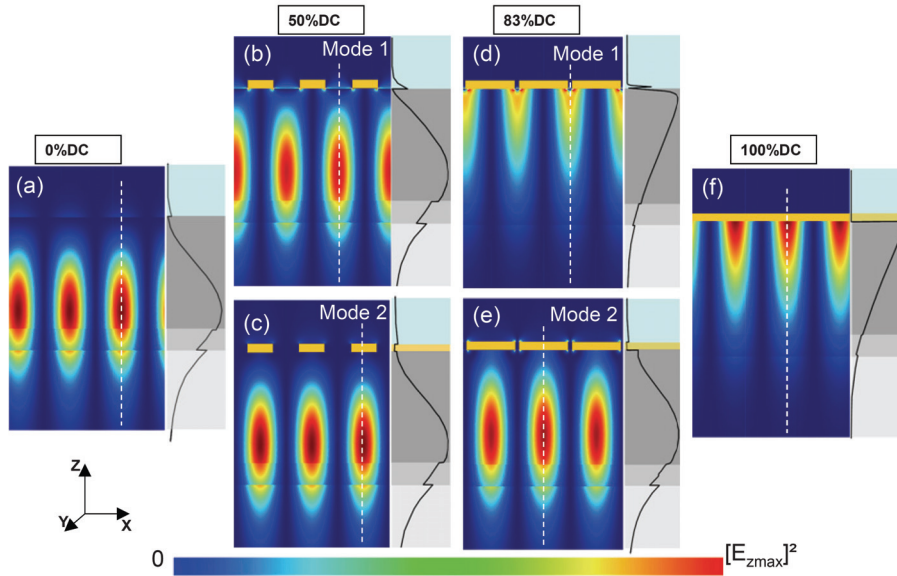
Fig. 2. Electromagnetic field distribution of the symmetric and anti-symmetric modes. Field plots of modes #1 and #2 for different grating duty cycles. The square modulus of E_z is shown. Mode #1 (top panels) is localized below the regions with no top metallization, while mode #2 (bottom panels) is localized below the metallic fingers. Panels (a) and (f) show the extreme cases of air-guided and pure surface-plasmon modes, respectively. In this case the modes are degenerate and therefore we show only one field plot. Panel (b) and panel (d) show that mode #1 is gradually pulled towards the metal with increasing duty cycle. The 1D cross-sections on the side (black lines) show that the maximum of the electric field shifts towards the metal-semiconductor interface with increasing DC. Panels (c) and (e) show the very different behavior of mode #2. With increasing duty cycles, the mode is not attracted towards the metal interface. The 1D cross-sections show in fact that - even at DC=83% - the maximum of the electric field is still localized in the active region, and not at the metal-semiconductor interface. Counter intuitively, it looks like mode #2 experiences confinement by air-claddings, although the DC is so high that almost the whole top surface is metalized.

from classical index guided DFBs, in which both modes at the band edge have practically equal losses.

The semi-transparent blue rectangle of Fig. 1(c) highlights an unexpected effect: as soon as the metal is patterned, a low loss waveguide mode suddenly appears. This phenomenon can be understood upon inspection of the electromagnetic field distribution of the modes. Figure 2 shows the calculated electric field intensity distribution in the xz plane for increasing values of grating DC (0%, 50%, 83%, and 100%, from left to right), and for modes #1 (top panels) and #2 (bottom panels). Panels (a) and (f) show the two extreme cases of air- and unpatterned surface-plasmon-guiding, respectively. Counter-intuitively, the low-loss mode #2 is not localized below the air-gaps, but it exhibits the field maxima below the metallic fingers. In particular, mode #1 is only gradually displaced from the metallic interface with decreasing grating duty-cycles (panels (d) to (b), and corresponding 1D sections), while mode #2 is immediately affected by even a minute air-slit 100-nm-wide. Comparison between panels (e) and (f) show that 100-nm-wide-slits are sufficient to repel the mode inside the semiconductor structure, with a consequent loss reduction. Note: the loss-reduction of mode #2 originates from a sudden modification of the

field distribution as soon as the metal is patterned. The following section provides an intuitive physical model to elucidate the sudden onset of this low-loss mode.

3. Physical discussion on the origin of the low-loss mode

The scheme in Fig. 3(a) shows a close up of the metal-semiconductor interface and corresponding field plot for E_z, of an unpatterned surface-plasmon structure (a standing wave is considered). A surface plasmon involves the physical motion of electric charges at the metal surface, which is also responsible for the (ohmic) SP propagation losses. After half a period the electric field direction will be reversed, and - in a first approximation - we can assume that charges will have moved following the dotted arrows: charge transfer occurs across the (nodal) regions of zero electric field in the z-direction (white dotted lines). If the top metal is pat-
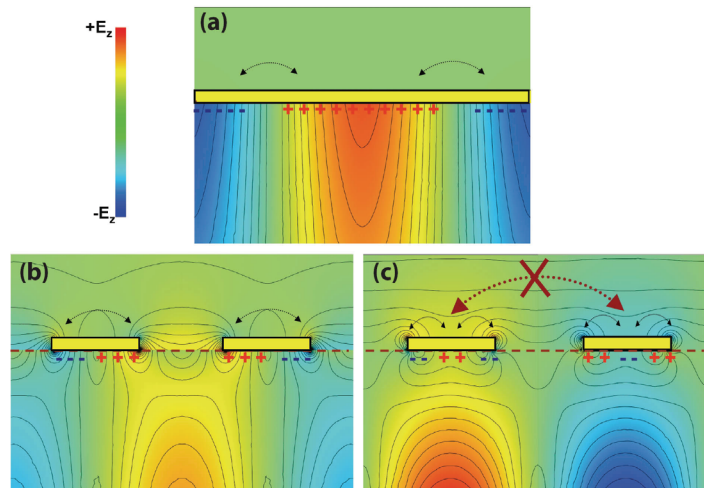

Fig. 3. Intuitive physical explanation of the loss-reduction effect. Schematic close-up of the metal-semiconductor interface of a surface-plasmon waveguide. The system is considered infinite in the y direction (x,y,z directions are defined as in Fig. 2). (a) The case of an unpatterned, continuous metal surface. If mirrors are placed at the left and right edges of the structure, a Fabry-Perot resonator is present and a standing surface-plasmon wave appears. The z component of such a wave is plotted in color scale, together with the surface charge density responsible for the SP. The corresponding charge oscillation is indicated by the dotted curved black arrows. The vertical white dotted lines mark the position of the nodal lines for E_z. Note: the charge oscillation always takes place across the nodal lines. (b), (c) The case of a 1st order grating patterned in the top metal surface only. A symmetric and an anti-symmetric mode appear. The symmetry is taken with respect to the center of the air slit. The symmetric mode (mode #1) exhibits nodal lines below the metallic fingers (panel (b)). The charge oscillation naturally takes place within the metallic fingers (dotted curved black arrows). The anti-symmetric mode (mode #2, panel (c)) on the other hand exhibits a nodal line between the metallic fingers. Naturally the charge oscillation should take place across the finger (dotted curved red arrow), but this is no more possible since the fingers are separated. The charges are therefore forced to oscillate within the metallic fingers but - for symmetry arguments - two points of zero electric field must exist at the metal surface. In this case however, the charge oscillation cannot be associated to a nodal line, since the wavelength is fixed. The anti-symmetric optical mode must accommodate this additional constraint: this is the physical mechanism underlying its anomalous behavior at very high duty-cycle values.

terned as a grating, symmetric and anti-symmetric modes will appear: in the first case the nodal lines are located below the metallic fingers (Fig. 3(b)), in the second case below the air gaps (Fig. 3(c)). Each single metallic finger must be electrically neutral. In the former case charges oscillate as schematized in Fig. 3(b) (black arrows), and correctly one nodal line is present where there is charge transfer. In the second case, however, no charge transfer can occur across since the nodal line is now located below the air gaps (Fig. 3(c), red crossed arrow). Charges must oscillate within each finger, and the simplest charge distribution imposed by symmetry is schematized in Fig. 3(c) (black arrows). However, in this case the charge oscillation cannot induce additional nodal lines, since this would require a different wavelength. The optical mode must adapt to allow for regions of zero electric field at the metal surface, and is moved into the substrate, as shown in Fig. 2(e). This is only an intuitive picture, but it describes correctly the physical mechanism underlying the observed effect.

Note: the presence of a bottom dielectric confinement layer (the InP substrate in this case) - acting as a low-loss effective mirror - is crucial [17]. Similar full metallic gratings have been in fact employed for THz 2nd order DFB lasers [21, 22, 23]. However, the use of metal-metal waveguides - which employ a metallic mirror to confine light on the substrate side too - prevents in that case the onset of the low-loss mode, since both modes, symmetric and anti-symmetric, are of surface-plasmon nature.

4. Implementation on a mid-infrared semiconductor laser

We have fabricated mid-infrared surface-plasmon QC lasers making use of an air-metal top grating for distributed feedback. An SEM image of a typical device is shown in Fig. 4(a). E-beam lithography and a lift-off process have been used to deposit 50%-duty-cycle, Ti/Au (3/200-nm-thick) gratings with different periods on the top surface of the sample. The gratings are typically 20 μm wide and a few millimeters long. Ridge waveguide resonators are then fabricated by standard contact optical lithography and wet chemical etching. The wafers were grown in a vertical-reactor, low-pressure MOVPE system. Our growth conditions lead to an InGaAs and an AlInAs growth rate of around 1.8 ML/s for the active region. The sample contains 50 repeats of the same active region as in Ref. [18]. The stack of active regions+injectors is sandwiched between doped thin, top InGaAs contact facilitating layers and a bottom 0.5-μm-thick InGaAs cladding layer, n-doped 5x10^{16} cm^{-3}. The sample is grown on a low-doped (n=10^{17} cm^{-3}) InP substrate. To optimally overlap the frequencies of modes #1 and #2 with the optical gain, several devices were fabricated with grating periods Λ ranging from 1.16 μm to 1.25 μm.

Fig. 4(b) shows laser spectra at several temperatures for two devices with different grating periods (black and red curves, respectively). Spectra are plotted in reduced frequency Λ/λ. For an optimized overlap between gain and grating periodicity the devices exhibit single mode emission up to injection currents twice/thrice the threshold current density (J_{th}), with a side-mode suppression ratio of at least 30 dB (Fig. 4(c), inset). The emission wavelength shift of 0.4 nm/K allows us to assign the feedback mechanism to the presence of the surface grating. All the devices lase at room temperature, either at $\Lambda/\lambda \approx 0.157$ or at $\Lambda/\lambda \approx 0.159$. These values are in reasonable good agreement with the position of the modes for a 50% DC grating, as in Fig. 1(b). We assign therefore the emission at $\Lambda/\lambda = 0.157$ to mode #1, and the one at $\Lambda/\lambda = 0.159$ to mode #2. Fig. 4(c) shows the J_{th} as a function of the heat-sink temperature for a 100% (unpatterned SP), 50% and 0% duty-cycle surface-plasmon DFB lasers fabricated from the same wafer. In qualitative agreement with the theory (Fig. 1(c)) the grating reduces the optical losses with respect to a standard, unpatterned SP waveguide. The 0% DC device is not improved with respect to the 50% DC one: at 0% DC the current is injected from lateral contacts only [20], and non-uniform current injection explains why a further J_{th} reduction is not observed.

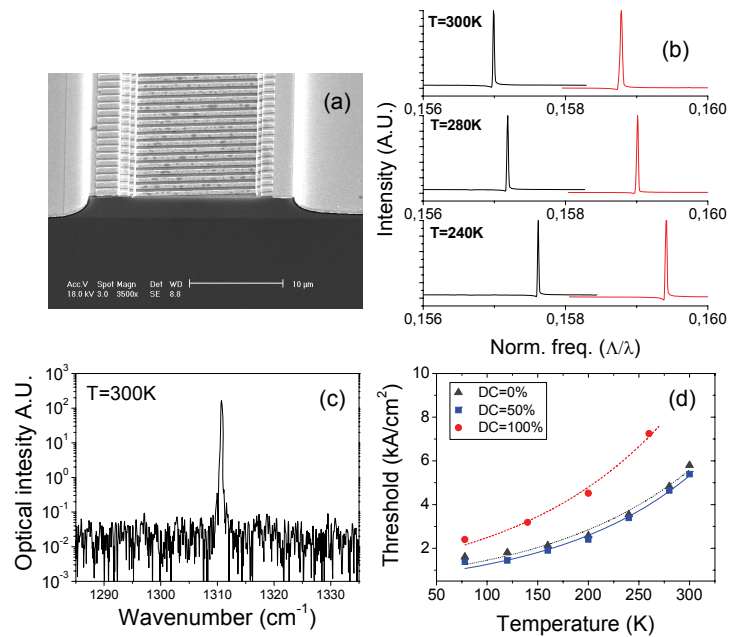The interest of this technology lies in the simplification. While devices based on standard

Fig. 4. Spectral and laser threshold characterizations. (a) SEM image of a typical device. The electric current is injected into the device active region, then through the substrate via the patterned metallic top contact. A layer of Si_xN_y is deposited on the whole sample - except the device top surface - for electrical insulation. (b) Typical laser spectra at $T = 240K$, $280K$ and $300K$ for two devices with different grating periods (black and red curves, respectively). The spectra are plotted in reduced frequency Λ/λ. Comparison with the band-structure simulations allows us to assign the room-temperature (RT) emission at $\Lambda/\lambda = 0.157$ to mode #1, and the one at $\Lambda/\lambda = 0.159$ to mode #2. (c) Threshold current densities as a function of the heat-sink temperature for a typical un-patterned surface-plasmon QC laser (red), for a 50% duty-cycle (blue) and for a 0% duty-cycle (dark grey) surface-plasmon DFB laser fabricated from the same epitaxial material. The dotted lines are exponential fits to the points. The data presented for the 50% DC device refer to mode #2, but we did not find much difference in threshold between mode #1 and mode #2. We believe this is due to higher than expected material-losses, which - for a 50% DC - reduce the loss difference between the two modes. Initial measurements on 70% DC devices (data not shown) indicate that they lase only on mode #2, in agreement with the theory which predicts the largest loss difference between the modes at 80% DC. Inset: Typical single mode emission of a DFB device in log-lin scale. A side-band suppression ratio of at least 30 dB is obtained.

waveguides exhibit better performances, SP DFB lasers allow one to implement an efficient distributed-feedback by simply structuring the metallic surface, for applications that require pulsed, room-temperature operation. In the future, the use of high-performance material should allow us to further improve the performances.

5. Near Field observation of electrically generated surface-plasmons

In the context of surface-plasmonics these results pave the way to the generation of plasmonic excitations in compact semiconductor laser devices operating under electrical injection. In a non-semiconductor system, initial observations have been reported using an organic LED (OLED) and leakage radiation microscopy [14, 24]. The interest of a semiconductor system lies on one hand in the compatibility with micro-electronics, on the other hand on the possibility of exploiting the high optical gains typical of semiconductor lasers. In addition we provide di-

AFM Topography aSNOM (xy section) aSNOM (xz section) Simulation (xz section)
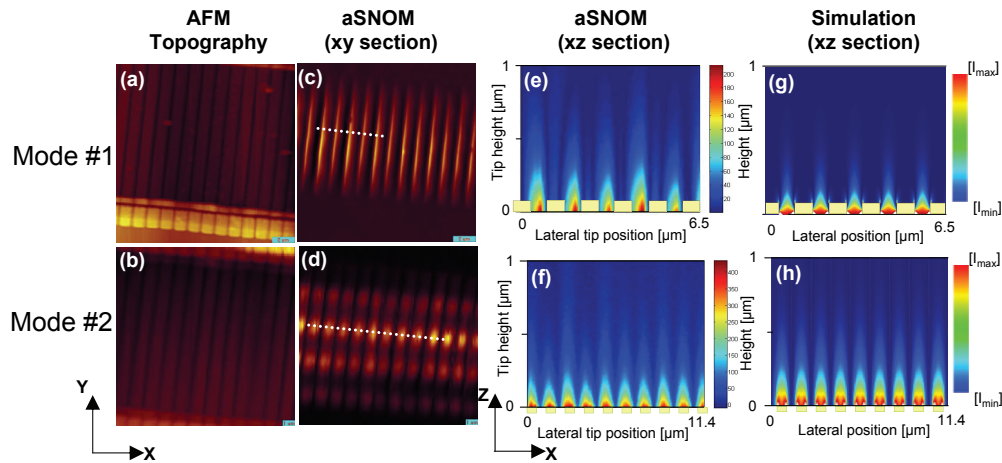
Mode #1

Mode #2

Fig. 5. Near-field characterizations. Apertureless near-field optical microscopy (a-NSOM) survey of the field distribution at the surface of two surface plasmon DFB lasers. The top row reports the results for a device operating on mode #1 ($\Lambda/\lambda = 0.157$), while the bottom row focuses on a device lasing on mode #2 ($\Lambda/\lambda = 0.159$). (a),(b): AFM topography of the two samples. (c),(d): a-NSOM images recorded simultaneously with the AFM images of panels (a) and (b). The demodulation is performed at the tip oscillation frequency. The comparison with the AFM images shows that when the laser operates on mode #2 the electric field is localised on the top metal-air interface. (e),(f): Vertical cross-sections in the xz plane (axes definition at the bottom left) of the a-NSOM signal corresponding to the white dotted lines in panels (c) and (d). The grating metallic fingers are indicated by the yellow semi-transparent rectangles. The maximum of the electric field is located at the semiconductor-air interface or at the metal-air interface, for lasers operating on mode #1 or mode #2, respectively. (g),(h): Numerical simulations corresponding to the measurements reported in panels (e), (f). The value of $|E_z|^2$ is reported. The laser operating at $\Lambda/\lambda = 0.157$ exhibits the electric field maximum in the gaps between the metallic fingers. In contrast, the device lasing at $\Lambda/\lambda = 0.159$ exhibits an evanescent electric field onto the metallic fingers, with a confinement decay length of ≈ 300 nm in the z-direction. The agreement between the theory and the a-NSOM experimental measurements is excellent.

rect, real-space observation of surface-plasmon generation via apertureless near-field scanning optical microscopy (a-NSOM). The a-NSOM is a unique technique to unravel the spatial distribution of electromagnetic modes of surface plasmons [25] and also of semiconductor lasers [26, 27, 28].

Figure 5 presents the result of the a-NSOM characterization of the field distribution at the top surface of two devices, one lasing on mode #1 ($\Lambda/\lambda = 0.157$), and a second one operating on mode #2 ($\Lambda/\lambda = 0.159$). Details of the measurement setup are given in Refs. [25, 28]. Figures 5(a) and 5(b) show topographical (AFM) images of the device top surface. Figure 5(c) and 5(d) show a-NSOM images acquired simultaneously with the AFM scans, with the QC devices in operation above laser threshold. A comparison with the AFM images clearly indicates that the near-field in the laser operating on mode #1 (Fig. 5(c)) exhibits maxima located in the gaps between the metallic stripes. On the contrary, the near-field associated with mode #2 (Fig. 5(d)) clearly exhibits field maxima located onto the gold metallic fingers which constitute the grating. These images unambiguously identify modes #1 and #2 as the active modes in the devices.

Figures 5(e) and (f) show instead the a-NSOM signal (demodulated at the tip oscillation frequency) acquired in the xz plane. The scans follow the white dashed lines in Figs. 5(c) and (d). This measurement allows one to asses the electric field decay length. Regardless of the

demodulation frequency, a decay length for the optical signal of ≈ 300 nm is observed in both devices, indicating that the electromagnetic field remains highly confined close to the grating structure. The results of numerical simulations [19] corresponding to the xz scans for mode #1 and #2 are plotted in Figs. 5(g) and (h): the theory is in excellent agreement with the near-field results.

As the laser emission is well below the plasma frequency, the evanescent field detected onto the metal surface reveals the presence of a SP, which owes its existence to the optical gain of the underlying laser active region. We have thus implemented a compact semiconductor device capable of generating SPs upon electrical injection. A detail should be noted: our approach does not require a metallic layer with a thickness of the order of the skin-depth to allow for SP coupling. The grating itself acts as a tunnel coupler, and a thick metal - which is a necessary requirement for realistic injection devices - can be employed.

Finally, Fig. 5(h) shows that the experimental decay length of the evanescent electric field is shorter than for a normal SP propagating on a plain metal/air interface. A $\lambda = 7.5\ \mu$m SP wave at a plain gold-air interface should exhibit a decay length of several microns [2]. This case is different: the detected intensity comes from the tail of the optical mode inside the cavity that tunnels out through the metal layer. It has been pointed out in Ref. [29] that a proper patterning of the metallic surface allows one to engineer the SP decay length by design. The existence of these artificially designed SPs has been recently confirmed experimentally [30]. An analogous phenomenon takes place in our system, thanks to the combined effect of the surface patterning and of the coupling to the underlying asymmetric waveguide.

6. Conclusions

We have presented detailed measurements which unambiguously show surface-plasmon generation via electrical injection with a compact semiconductor laser device. The underlying principle is that the electrical injection drives the (QC) laser source, which in turn operates on a surface-plasmon mode. The extension of this concept to shorter visible and telecom wavelengths should be possible, with of course proper waveguide modifications in order to take into account the much higher metal losses in the near-infrared. This could lead to the demonstration of compact plasmon generators which could be integrated in plasmonic circuits [8, 9].